



**U.S. Army  
Research Institute of  
Environmental Medicine**

*Natick, Massachusetts*

**TECHNICAL REPORT NO. T20-07  
DATE April 2020**

**DEVELOPMENT OF A METHOD FOR THERMAL SIMULATIONS USING USARIEM  
AVATARS IN COMSOL MULTIPHYSICS®**

**Approved for Public Release; Distribution is Unlimited**

**United States Army  
Medical Research & Development Command**

## **DISCLAIMER**

The opinions or assertions contained herein are the private views of the author(s) and are not to be construed as official or reflecting the views of the Army or the Department of Defense. The investigators have adhered to the policies for protection of human subjects as prescribed in 32 CFR Part 219, Department of Defense Instruction 3216.02 (Protection of Human Subjects and Adherence to Ethical Standards in DoD-Supported Research) and Army Regulation 70-25.

**USARIEM TECHNICAL REPORT T20-07**

**DEVELOPMENT OF A METHOD FOR THERMAL SIMULATIONS USING USARIEM  
AVATARS IN COMSOL MULTIPHYSICS®**

Diana P. Sanford  
Gary P. Zientara

Biophysics and Biomedical Modeling Division

April 2020

U.S. Army Research Institute of Environmental Medicine  
Natick, MA 01760-5007

**REPORT DOCUMENTATION PAGE**

*Form Approved  
OMB No. 0704-0188*

The public reporting burden for this collection of information is estimated to average 1 hour per response, including the time for reviewing instructions, searching existing data sources, gathering and maintaining the data needed, and completing and reviewing the collection of information. Send comments regarding this burden estimate or any other aspect of this collection of information, including suggestions for reducing the burden, to Department of Defense, Washington Headquarters Services, Directorate for Information Operations and Reports (0704-0188), 1215 Jefferson Davis Highway, Suite 1204, Arlington, VA 22202-4302. Respondents should be aware that notwithstanding any other provision of law, no person shall be subject to any penalty for failing to comply with a collection of information if it does not display a currently valid OMB control number.

**PLEASE DO NOT RETURN YOUR FORM TO THE ABOVE ADDRESS.**

<b>1. REPORT DATE (DD-MM-YYYY)</b>		<b>2. REPORT TYPE</b>		<b>3. DATES COVERED (From - To)</b>	
<b>4. TITLE AND SUBTITLE</b>			<b>5a. CONTRACT NUMBER</b>		
			<b>5b. GRANT NUMBER</b>		
			<b>5c. PROGRAM ELEMENT NUMBER</b>		
<b>6. AUTHOR(S)</b>			<b>5d. PROJECT NUMBER</b>		
			<b>5e. TASK NUMBER</b>		
			<b>5f. WORK UNIT NUMBER</b>		
<b>7. PERFORMING ORGANIZATION NAME(S) AND ADDRESS(ES)</b>				<b>8. PERFORMING ORGANIZATION REPORT NUMBER</b>	
<b>9. SPONSORING/MONITORING AGENCY NAME(S) AND ADDRESS(ES)</b>				<b>10. SPONSOR/MONITOR'S ACRONYM(S)</b>	
				<b>11. SPONSOR/MONITOR'S REPORT NUMBER(S)</b>	
<b>12. DISTRIBUTION/AVAILABILITY STATEMENT</b>					
<b>13. SUPPLEMENTARY NOTES</b>					
<b>14. ABSTRACT</b>					
<b>15. SUBJECT TERMS</b>					
<b>16. SECURITY CLASSIFICATION OF:</b>			<b>17. LIMITATION OF ABSTRACT</b>	<b>18. NUMBER OF PAGES</b>	<b>19a. NAME OF RESPONSIBLE PERSON</b>
<b>a. REPORT</b>	<b>b. ABSTRACT</b>	<b>c. THIS PAGE</b>			<b>19b. TELEPHONE NUMBER (Include area code)</b>

## TABLE OF CONTENTS

<u>Section</u>	<u>Page</u>
List of Figures.....	iv
List of Tables.....	iv
Acknowledgments .....	v
Executive Summary .....	1
Introduction .....	2
Methods .....	2
Conversion of 2 mm FE standard anatomy into voxel format .....	2
Automated modification of the volumetric representation .....	5
Manual modification of the volumetric representation.....	9
Conversion of the volumetric data back into a mesh format .....	10
Computation of the stationary temperature profile .....	11
Results .....	13
Thermal Simulation.....	13
Model Validation .....	14
Discussion.....	15
Conclusions.....	16
References.....	17

## LIST OF FIGURES

<u>Figure</u>		<u>Page</u>
1	Volumetric representation of the 2 mm standard anatomy with 31 merged tissue types. The skin, fat and muscle are shown in green, yellow and maroon, respectively. All other tissues are hidden for clarity.	5
2	Volumetric representation of the 2 mm standard anatomy with 31 merged tissue types after code modification. The (A) skin, (B) fat and (C) muscle/bone layers are shown in green, yellow and maroon/blue, respectively.	8
3	Volumetric representation of the 2 mm standard anatomy with 31 merged tissue types after code modification and manual segmentation. The (A) skin, (B) fat and (C) muscle/bone layers are shown in green, yellow and maroon/blue, respectively.	10
4	The temperature plot for (A) the surface and (B) a coronal slice at $x = 100$ mm of the modified standard anatomy after stationary temperature simulation with an external temperature of $27^{\circ}\text{C}$ .	13

## LIST OF TABLES

<u>Table</u>		<u>Page</u>
1	Original 2mm Tissue Types	3
2	Mapping of the original 77 tissue types to 31 merged tissue types	4
3	Parameters for 31 tissue types from the IT'IS Foundation Database	12
4	Average temperatures of the 31 merged tissue types with an external temperature of $27^{\circ}\text{C}$	14
5	Comparison of the simulated temperatures to the measured temperatures from the literature	14

## **ACKNOWLEDGMENTS**

The authors would like to thank the following individuals for their assistance in preparing this technical report: Dr. Reed Hoyt and Dr. Scott Montain for their support of this effort and Dr. Adam Potter for his critical review of this technical report.

## **EXECUTIVE SUMMARY**

USARIEM has developed whole-body models, termed avatars, which are individualized 3D finite element (FE) models of Soldiers with complete internal anatomy. This report describes the methods used to convert a single avatar into a usable volumetric representation of a human that can be used for simulating responses to environmental factors. This current work specifically focuses on thermal simulations.

Validation of this model was performed by comparing the simulation results to published data. The current validation is conducted in thermoneutral conditions with an ambient temperature of 27°C. Data compared where the averages for the skin, fat, muscle, and esophagus. Errors for each of the measured tissues was less than 6.5% (skin, 3.31; fat, 6.32; muscle, 5.03; esophagus, 0.89).

This work demonstrates the capability of this modeling approach, in conjunction with this type of anatomical data, can be used to produce an FE mesh avatar that is compatible with thermal simulations.

## INTRODUCTION

Developing computational human models, or “virtual humans”, has been an increasingly active field with broad applications in medical device development (1, 2), automotive safety research (3-6) and electromagnetic and radiology studies (1, 7-9). Many of these applications employ partial human models, containing only the anatomy or region of interest. For example, a sub-millimeter model of the head and neck developed from medical images (10) has been widely used. However, the number of whole body models remains limited. The largest collection of anatomical models is the Virtual Population from the Foundation for Research on Information Technologies in Society (IT<sup>2</sup>S) Foundation, containing males and females with a variety of ages (11-13). A recent overview of anatomical whole body models can be found in Makarov et al. (14).

USARIEM has developed whole-body models, termed avatars, which are individualized 3D finite element (FE) models of soldiers with complete internal anatomy (15). Each avatar is generated by warping gender specific standard anatomy to match body surface scans of soldiers from the US Army Anthropometric Survey II (ANSUR II) database (16). While each avatar provides a complete anatomy description, we note that mesh generation software can cause inconsistencies within the meshes that make them incompatible in FE simulation packages. To resolve this issue, we describe a methodology to improve the mesh accuracy and make the mesh compatible with FE simulations in COMSOL Multiphysics<sup>®</sup>. The work in this report specifically focuses on thermal simulations.

## METHODS

### **Conversion of 2 mm FE standard anatomy into voxel format**

The volumetric representation of the Virtual Family male adult from the IT<sup>2</sup>S Foundation (11-13) was converted into 3D finite element (FE) mesh data as previously described (15). This FE dataset corresponds to a resolution of 2 mm and is represented by 6,757,775 vertices and a corresponding list of 11,765,362 faces and 41,170,347 tetrahedra elements generated using the iso2mesh software (17). The combination of the vertices, faces and tetrahedron elements describes the complete labeled internal anatomy, with 77 different tissue types (Table 1). Despite the detail of this dataset, there are several challenges in making this mesh compatible with FE simulations. These include individual tissue meshes that contain holes or gaps within their shell, meaning their surfaces are not completely interconnected (i.e., not ‘watertight’) and contain non-manifold triangle edges. Additionally, there are many smaller gaps or overlaps between tissues that result in complicated surface interactions. Therefore, in order to generate a model that is appropriate for FE simulations, several modifications need to be performed to the standard anatomy.

**Table 1. Original 2mm Tissue Types.**

Original 2 mm indices				
Original #	Index Description		Original #	Index Description
1	Adrenal gland		40	Liver
2	Air		41	Lung
3	Arteries		42	Mandible
4	Bladder		43	Marrow, red
5	Blood vessels		44	Medulla oblongata
6	Bone		45	Meniscus
7	Brain grey matter		46	Midbrain
8	Brain white matter		47	Mucous membrane
9	Bronchi		48	Muscle
10	Bronchi lumen		49	Nerve
11	Cartilage		50	Pancreas
12	Cerebellum		51	Patella
13	Cerebrospinal fluid		52	Penis
14	Commissure anterior		53	Pharynx
15	Commissure posterior		54	Pineal body
16	Connective tissue		55	Pons
17	Cornea		56	Prostate
18	Diaphragm		57	SAT
19	Ear cartilage		58	Skin
20	Ear Skin		59	Skull
21	Epididymis		60	Small intestine
22	Esophagus		61	Small intestine lumen
23	Esophagus lumen		62	Spinal cord
24	Eye lens		63	Spleen
25	Eye sclera		64	Stomach
26	Eye vitreous humor		65	Stomach lumen
27	Fat		66	Teeth
28	Gallbladder		67	Tendon / ligament
29	Heart lumen		68	Testis
30	Heart muscle		69	Thalamus
31	Hippocampus		70	Thymus
32	Hypophysis		71	Thyroid gland
33	Hypothalamus		72	Tongue
34	In vertebral disc		73	Trachea
35	Kidney cortex		74	Trachea lumen
36	Kidney medulla		75	Ureter
37	Large intestine		76	Veins
38	Large intestine lumen		77	Vertebrae
39	Larynx			

In order to allow for systematic manipulation of the dataset, the FE mesh standard anatomy was converted into the volumetric representation. To do this, the labels corresponding to the 77 tissue types were sorted from largest to smallest, in an attempt to ensure that small structures will not be overwritten in the volumetric

representation. Subsequently, all the components are looped over in the order previously described; the raw vertices and tetrahedral data are added to the corresponding voxel in the volumetric data. With a 2 mm voxel edge length, there are 305, 155 and 930 bins in the x, y and z directions, respectfully. In the volumetric data, each voxel is labeled with the corresponding tissue type.

To further simplify the volumetric dataset, tissues with similar properties were combined and merged into 31 tissue types (Table 2). A 77x2 mapping array was created, corresponding to the original 77 tissues types and the new 31 merged tissue types. For example, arteries, blood vessels and veins were combined to form a single tissue type of blood. The volumetric representation is shown in Figure 1.

**Table 2:** Mapping of the original 77 tissue types to 31 merged tissue types.

Merged Index	Merged Tissue type	Original 2 mm indices
1	Skin	20: Ear Skin ;58: Skin
2	Fat	27: Fat ;57: SAT
3	Muscle / Tendon / Ligament	16: Connective tissue; 18: Diaphragm; 48: Muscle; 67: Tendon / ligament
4	Bone / Cartilage	6: Bone; 11: Cartilage; 19: Ear cartilage; 34: Invertebral disc; 39: Larynx; 42: Mandible; 43: Marrow, red; 45: Meniscus; 51: Patella; 59: Skull; 66: Teeth; 77: Vertebrae
5	Air	2: Air; 53: Pharynx
6	Blood	3: Arteries; 5: Blood vessels; 76: Veins
7	Mucous membrane	47: Mucous membrane
8	Lungs	41: Lung
9	Heart	29: Heart lumen; 30: Heart muscle
10	Liver	40: Liver
11	Kidneys	35: Kidney cortex; 36: Kidney medulla
12	Stomach	64: Stomach; 65: Stomach lumen
13	Pancreas	50: Pancreas
14	Gallbladder	28: Gallbladder
15	Bladder	4: Bladder; 75: Ureter
16	Spleen	63: Spleen
17	Large intestine	37: Large intestine; 38: Large intestine lumen
18	Small intestine	60: Small intestine; 61: Small intestine lumen
19	Esophagus	22: Esophagus; 23: Esophagus lumen
20	Trachea	73: Trachea; 74: Trachea lumen
21	Bronchi	9: Bronchi; 10: Bronchi lumen
22	Eyes	17: Cornea; 24: Eye lens; 25: Eye sclera; 26: Eye vitreous humor
23	Tongue	72: Tongue
24	Brain	7: Brain grey matter; 8: Brain white matter; 12: Cerebellum; 13: Cerebrospinal fluid; 14: Commissura anterior; 15: Commissura posterior; 31: Hippocampus; 32: Hypophysis; 33: Hypothalamus; 44: Medulla oblongata; 46: Midbrain; 54: Pineal body; 55: Pons; 69: Thalamus
25	Spinal Cord / Nerve	49: Nerve; 62: Spinal cord
26	Adrenal gland	1: Adrenal gland
27	Thyroid gland	71: Thyroid gland
28	Thymus	70: Thymus
29	Testis / Epididymis	21: Epididymis; 68: Testis
30	Prostate	56: Prostate
31	Penis	52: Penis

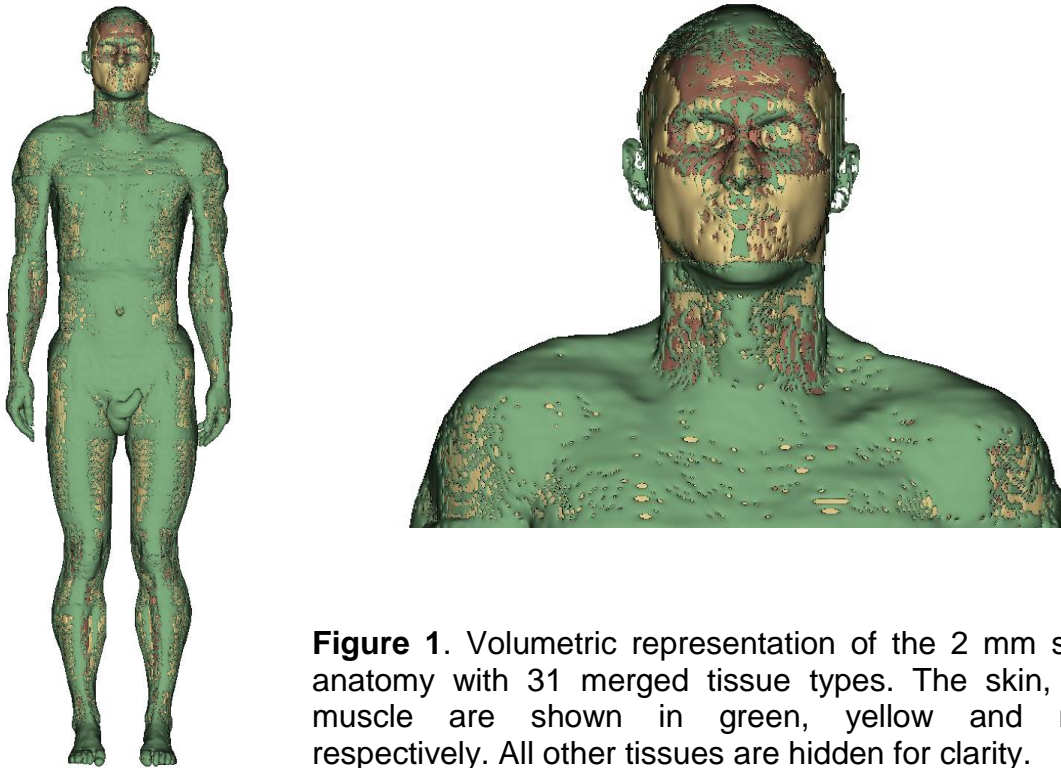


**Figure 1.** Volumetric representation of the 2 mm standard anatomy with 31 merged tissue types. The skin, fat and muscle are shown in green, yellow and maroon, respectively. All other tissues are hidden for clarity.

### Automated modification of the volumetric representation

From Figure 1, it is clear that the tissues have spaces with unconnected elements, creating gaps in their surface. These gaps make the meshes incompatible with FE simulations. To address this issue, MATLAB® code was written to eliminate the holes within the mesh, remove any small isolated ‘islands’ and ensure the skin and fat are represented as continuous tissues. The automated modification process can also be described as a series of morphological image processing operations, including dilation and erosion. This process is done in nine general coding steps as follows:

- (1) First, a check is done to see if there are any isolated voxels. For each voxel, the indices of the six surrounding voxels are checked: (1–4) The four voxels in the same  $x/y$  plane which each share an edge with the voxel of interest and (5–6) the two voxels in the adjacent  $z$  planes on the top and bottom of the voxel of interest. If all six of the checked voxels have the same index, the index of the voxel of interest is changed to match the index of the six voxels.
- (2) Next, an additional check for isolated voxels within the same  $z$  layer is performed. For each voxel, the indices of the 8 surrounding voxels are checked: (1–4) The four voxels in the same  $x/y$  plane which each share an edge with the voxel of interest and (5–8) the four voxels in the same  $x/y$  plane which share a corner with the voxel of interest. If all eight of the checked

voxels have the same index, the index of the voxel of interest is changed to match the index of the eight voxels.

(3) Ensuring the skin is a complete structure surrounding the outside of the body is done using two steps:

(a) For each  $z$  layer, the voxels corresponding to the edge of the labeled tissues are identified. This corresponds to the minimum and maximum labeled voxel for each  $x$  and  $y$  layer, such that the labeled voxel is next to an unlabeled voxel. The voxels corresponding to the edge of the labeled tissues are changed to skin, if they were not already labeled as such. Note that this method assumes that there are no holes in the body and that the entire outside of the body is a layer of skin.

(b) To ensure connectivity between the skin voxels in (a) above, a voxel of interest is identified if a skin voxel is next to an unlabeled voxel. For a given  $z$  layer, the labels of the two voxels sharing a corner with the skin voxel on the opposite side as the unlabeled voxel are checked. If both checked voxels are also labeled as skin, the voxel sharing an edge with the skin voxel of interest and sharing an edge with both checked corners is updated to skin. There are four corner cases that must be checked, equivalent to the minimum in the  $x$  and  $y$  directions and maximum in the  $x$  and  $y$  directions.

(4) Ensuring the fat is a complete structure as a next layer on the inside of the skin is done similar to the skin modification; in two steps:

(a) For each  $z$  layer, the voxels corresponding to the interior of the skin layer are identified. This corresponds to the minimum and maximum labeled voxel for each  $x$  and  $y$  layer, such that the labeled voxel is next to a voxel labeled skin. The voxels corresponding to the edge of the labeled tissues are changed to fat, if they were not already labeled as such. Note that this method assumes that the fat is the next layer within the skin and is a completely connected structure.

(b) To ensure connectivity between the fat voxels in (a) above, a voxel of interest is identified if a fat voxel is next to a skin voxel. For a given  $z$  layer, the labels of the two voxels sharing a corner with the fat voxel on the opposite side as the skin voxel are checked. If both checked voxels are also labeled as fat, the voxel sharing an edge with the fat voxel of interest and sharing an edge with both checked corners is updated to fat. There are four corner cases that must be checked, equivalent to the minimum in the  $x$  and  $y$  directions and maximum in the  $x$  and  $y$  directions. Note that skin will not be overwritten as fat in this case.

(5) Another check for isolated voxels is done for each  $z$  layer. For each voxel, the indices of the 8 surrounding voxels are checked: (1–4) The four voxels in the

same  $x/y$  plane which each share an edge with the voxel of interest and (5–8) the four voxels in the same  $x/y$  plane which share a corner with the voxel of interest. If all eight of the checked voxels have the same index, the index of the voxel of interest is changed to match the index of the eight voxels. This process is iteratively performed on each  $z$  layer until no additional isolated voxels are found.

- (6) For each of the internal tissues, a check is done to identify single isolated patches of two or less voxels. This is done in two steps:
  - (a) First, a check for isolated voxels within the same  $z$  layer is performed. For a voxel of interest, the indices of the four voxels in the same  $x/y$  plane which each share an edge with the voxel of interest are checked. If the index of the voxel of interest is not the same as any of the four surrounding voxels, the index of the voxel of interest is changed to the mode of the four surrounding voxels.
  - (b) Second, a check for patches of two voxels within the same  $z$  layer is performed. For a given voxel of interest, the indices of the eight surrounding voxels are checked: (1–4) The four voxels in the same  $x/y$  plane which each share an edge with the voxel of interest and (5–8) the four voxels in the same  $x/y$  plane which share a corner with the voxel of interest. If only one of the eight indices is the same as the voxel of interest, both the voxel of interest and the voxel with the same index as the voxel of interest are changed to the mode of indices 1–4.
- (7) For each of the internal tissues, a check is done for voxels surrounded on three sides by the same tissue. For a voxel of interest, the indices of the four voxels in the same  $x/y$  plane which each share an edge with the voxel of interest are checked. If three of the checked indices are the same and not equal to the index of the voxel of interest, the index of the voxel of interest is updated to match that of the three checked indices.
- (8) For each of the internal tissues, a check is done for voxels that form an isolated L-shape containing three voxels within the same  $z$  layer. First, a corner is identified such that the voxel of interest is connected by an edge to two other voxels that each only have one connection with the same index. All three voxels are then updated to the mode of the indices of the eight voxels in the same  $x/y$  plane surrounding the voxel of interest.
- (9) Lastly, a final check is done to ensure there are not any additional single voxel or two voxel tissues present. This is done by looping over the internal tissues in the following two steps:
  - (a) Another check for patches of two voxels within the same  $z$  layer is performed. For a given voxel of interest, the indices of the eight surrounding voxels are checked: (1–4) The four voxels in the same  $x/y$

plane which each share an edge with the voxel of interest and (5–8) the four voxels in the same  $x/y$  plane which share a corner with the voxel of interest. If only one of the eight indices is the same as the voxel of interest, both the voxel of interest and the voxel with the same index as the voxel of interest are changed to the mode of indices 1–4.

- (b) A last check for isolated voxels within the same  $z$  layer is performed. For a voxel of interest, the indices of the four voxels in the same  $x/y$  plane which each share an edge with the voxel of interest are checked. If the index of the voxel of interest is not the same as any of the four surrounding voxels, the index of the voxel of interest is changed to the mode of the four surrounding voxels.

The volumetric representation of the skin, fat and muscle/bone after the in-house modification code is shown in Figure 2.

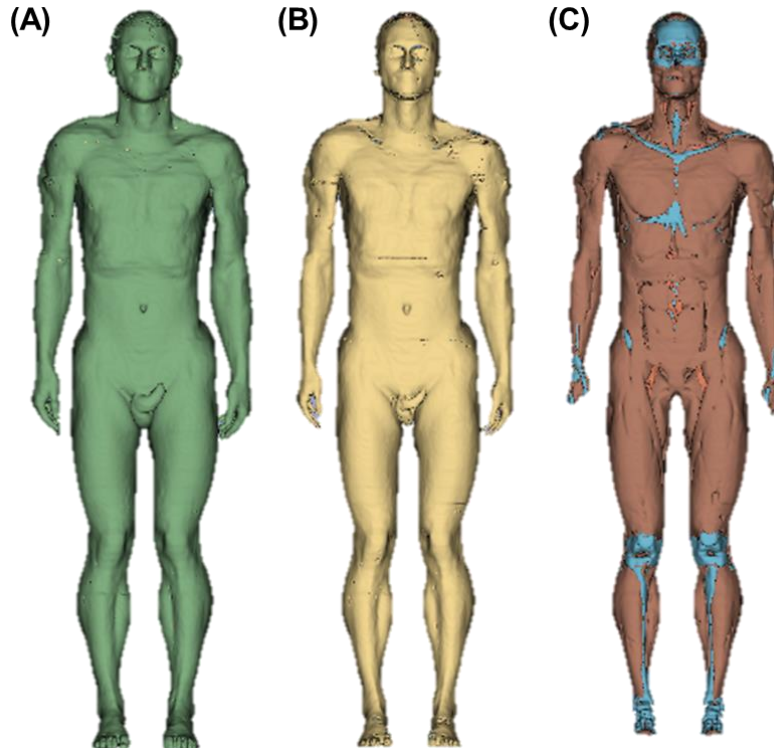


**Figure 2.** Volumetric representation of the 2 mm standard anatomy with 31 merged tissue types after code modification. The (A) skin, (B) fat and (C) muscle/bone layers are shown in green, yellow and maroon/blue, respectively.

## **Manual modification of the volumetric representation**

Modification of the volumetric representation using the in-house code greatly improved the quality of the mesh (Figure 2 compared to Figure 1). However, several holes still existed in each of the tissue meshes that require fixing prior to FE simulations. To do this, manual segmentation of the tissues in the volumetric representation was performed in 3D Slicer (18, 19). This manual segmentation process for 930 axial slices requires extensive time investment (i.e., months of people-hours) to generate an acceptable and watertight mesh.

The code modified version of the volumetric representation of the 2 mm standard anatomy is first saved as a series of image files and subsequently loaded into 3D Slicer for manual segmentation. 3D Slicer displays a three-dimensional representation of each tissue, simplifying the process of identifying holes and inconsistencies in the volumetric representation. First, each tissue is individually displayed and modified to fill all holes and ensure complete connectivity. Next, the muscle and fat tissues were simplified to eliminate small fat patches that are interspersed throughout the muscle tissue. This was done by making the fat a single layer underneath of the skin (may be many voxels deep depending on the location) and making a layer of fat surrounding the organs. After completion of the manual segmentation, the volumetric representation is saved as a nearly raw raster data (nrrd) file. The volumetric representation of the skin, fat and muscle/bone after the in-house modification code and manual modification is shown in Figure 3.

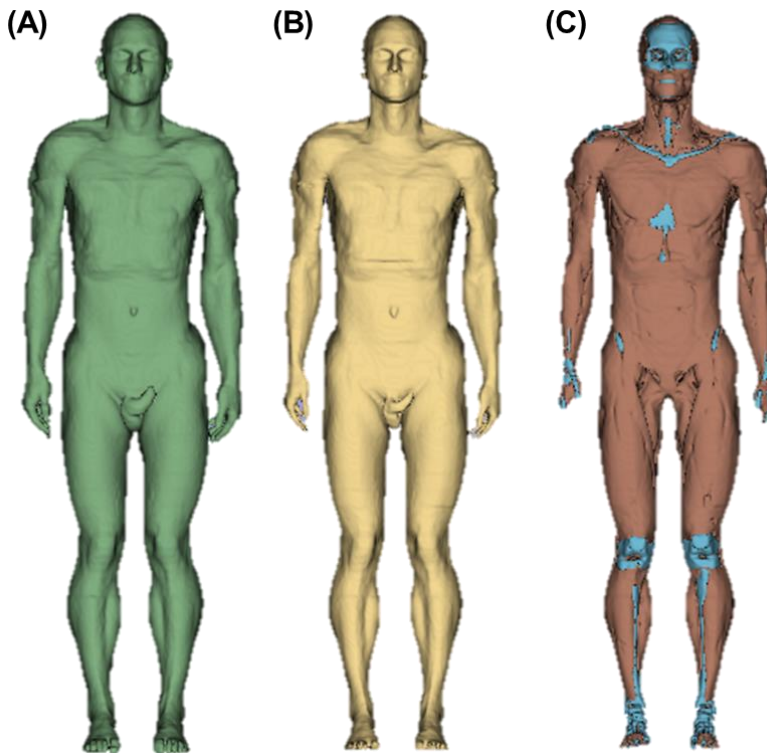


**Figure 3.** Volumetric representation of the 2 mm standard anatomy with 31 merged tissue types after code modification and manual segmentation. The **(A)** skin, **(B)** fat and **(C)** muscle/bone layers are shown in green, yellow and maroon/blue, respectively.

### Conversion of the volumetric data back into a mesh format

The volumetric dataset, currently stored in the nrrd format needs to be converted back into a FE mesh for simulation. This conversion is completed using the iso2mesh software (17). A built-in function, vol2mesh, converts a multi-valued volume to a tetrahedral mesh. Several inputs are required including the volume, number of voxels in the  $x/y/z$  direction, the target maximum tetrahedral element volume size (*volmax*), the maximum surface element size (*radbound*), the minimum angle of a surface triangle (*angbound*) and the maximum distance between the center of the surface bounding circle and the center of the element bounding sphere (*distbound*), a flag to indicate whether or not mesh validation and repair is performed, and the method for mesh generation. Herein, *volmax*, *radbound*, *angbound*, *distbound*, flag for repair and mesh generation method were set to 1.0, 1.0, 30.0, 1.0, “yes” to repair and *cgalmesh*, respectively. The mesh generation outputs a set of vertices, faces and tetrahedra, where the faces and tetrahedra are labeled with the correct tissue index.

After mesh generation, the  $x$ ,  $y$  and  $z$  dimensions were multiplied by the voxel dimension (2.0 mm) to ensure the mesh is scaled back to the correct standard anatomy size. Subsequently, the vertices, faces and tetrahedra are saved into a Nastran mesh format. The Nastran format supports the association of vertices with faces and

tetrahedra, greatly improving the ease of import into COMSOL Multiphysics® (20). The whole body mesh contains 6,531,918 vertices, 8,537,950 faces and 39,561,280 tetrahedra.

### Computation of the stationary temperature profile

A 3D stationary simulation using the Bioheat Transfer module of COMSOL Multiphysics® version 5.4 (21) was used to calculate the temperature profile of the modified standard anatomy. Heat transfer physics for a time dependent problem are modeled using the heat equation (Eq. 1).

$$\rho C_p \frac{\partial T}{\partial t} - \nabla \cdot (k \nabla T) = Q \quad (\text{Eq. 1})$$

where  $\rho$  is the density,  $C_p$  is the heat capacity,  $k$  is the thermal conductivity and  $Q$  is the heat source.

After opening a new model, the Nastran mesh is loaded into the Mesh 1 node of Component 1. The Nastran mesh imports both mesh and material data. Once loaded, there are 31 Import ID's created, corresponding to the 31 merged tissue types (Table 2). After import and finalization, the length unit is changed to mm in the Geometry node.

Subsequently, the Definitions node is used to add domain probes to compute the average temperature for each tissue. For example, a domain probe for the skin will have a selection with "ID 1 Import 1", corresponding to the merged index value for skin. Next, the materials node is used to add in a material for each of the 31 tissue types. Sticking with skin as an example, the selection will also be "ID 1 Import 1" and the geometric entity level is Domain. The material contents are specified for each tissue, and include thermal conductivity, density and heat capacity. The parameters for all 31 tissues are derived from the IT'IS Foundation Database (22) and given in Table 3. Note that the original tissue index and tissue identity for the merged tissue parameters are shown in the last column of Table 3.

**Table 3:** Parameters for 31 tissue types from the IT'IS Foundation Database.

Merged Index	Density (kg/m <sup>3</sup> )	Heat capacity (J/kg·K)	Thermal conductivity (W/m·K)	Blood perfusion rate (1/s)	Metabolic heat source rate (W/m <sup>3</sup> )	Original IT'IS Foundation parameter index <sup>a</sup>
1	1109.00	3390.5	0.372	1.97E-03	1827.10	58: Skin
2	911.00	2348.3	0.211	4.97E-04	461.48	27: Fat
3	1090.40	3421.2	0.495	6.68E-04	988.04	48: Muscle
4	1908.00	1312.8	0.320	3.18E-04	295.49	6: Bone
5	1.16	1003.7	0.027	0.00E+00	0.00	2: Air
6	1049.75	3617.0	0.517	1.75E-01	0.00	3: Arteries
7	1102.00	3150.0	0.343	1.09E-02	10131.85	47: Mucous Membrane
8	394.00	3886.0	0.387	2.63E-03	2446.41	41: Lung
9	1080.80	3686.0	0.558	1.85E-02	42640.20	30: Heart muscle
10	1078.75	3540.2	0.519	1.55E-02	10712.89	40: Liver
11	1049.00	3587.0	0.528	6.77E-02	19331.78	35: Kidney cortex
12	1088.00	3690.0	0.525	8.35E-03	7756.31	64: Stomach
13	1086.50	3164.0	0.512	1.39E-02	12913.70	13: Pancreas
14	1070.50	3716.0	0.521	5.35E-04	497.36	28: Gallbladder
15	1086.00	3581.3	0.522	1.41E-03	1311.86	4: Urinary bladder wall
16	1089.00	3596.0	0.534	2.83E-02	26258.89	63: Spleen
17	1088.00	3654.5	0.542	1.39E-02	12893.95	37: Large intestine
18	1030.00	3595.0	0.493	1.76E-02	16370.23	60: Small intestine
19	1040.00	3500.0	0.527	3.29E-03	3060.21	22: Esophagus
20	1080.00	3568.0	0.487	6.30E-04	585.40	73: Trachea
21	1101.50	3306.0	0.462	4.37E-03	4064.26	9: Bronchi
22	1004.50	4047.0	0.595	0.00E+00	0.00	26: Eye vitreous humor
23	1090.40	3421.2	0.495	1.42E-03	1317.18	72: Tongue
24	1045.50	3630.0	0.513	9.73E-03	11883.73	46: Midbrain
25	1075.00	3630.0	0.513	2.87E-03	2669.30	62: Spinal cord
26	1027.50	3512.5	0.443	2.50E-02	23196.94	1: Adrenal gland
27	1050.00	3609.0	0.519	9.84E-02	91457.85	71: Thyroid gland
28	1023.00	3043.4	0.336	4.21E-03	3914.64	70: Thymus
29	1082.00	3778.0	0.515	3.60E-03	3348.17	21: Epididymis
30	1045.00	3760.0	0.512	6.86E-03	6378.36	56: Prostate
31	1101.50	3306.0	0.462	2.20E-04	204.71	52: Penis

<sup>a</sup> Indicates the index from original IT'IS Foundation 2 mm standard male dataset corresponding to the given parameters

In the Bioheat transfer node, the reference temperature was set to 27°C. There are several nodes nested underneath of the Bioheat transfer node that were populated in the following steps. A Biological tissues *subnode* was added in for each of the 31 tissue types. For example, for skin, the selection is the same as described previously, “ID 1 Import 1”. Additionally, the following parameters need to be provided for each tissue: arterial blood temperature, specific heat of blood, blood perfusion rate, blood density and metabolic heat source. The arterial blood temperature, specific heat of blood and blood density are the same for all tissues and have values of 310.15 K, 3617 J/kg·K and 1049.75 kg/m<sup>3</sup>, respectively. The blood perfusion rate and metabolic heat source values for each tissue are shown in Table 3.

In the initial values *subnode*, the initial temperature for all domains was set to 37°C. Lastly, a heat flux *subnode* was added for all boundaries. Convective heat flux ( $q_0$ ) was modeled for the surface boundaries using Eq. 2, with a heat transfer coefficient ( $h$ ) equal to 15 W/m<sup>2</sup>·K and an external temperature ( $T_{\text{ext}}$ ) of 27°C.

$$q_0 = h \cdot (T_{\text{ext}} - T) \quad (\text{Eq. 2})$$

Note: settings and parameters not specified herein were left as default values.

## RESULTS

### Thermal Simulation

The stationary temperature simulation of the modified standard anatomy was computed with an external temperature of 27°C. The surface temperature plot of the modified anatomy is shown in Figure 4A. The temperature profile for a coronal slice through the center of the body ( $x = 100$  mm) is shown in Figure 4B. The hands, feet, ears and nose are the coldest after the stationary simulation. Average temperatures for the 31 merged tissue types are given in Table 4. The skin has the lowest temperature, 34.31°C, while the heart has the highest temperature, 37.58°C.

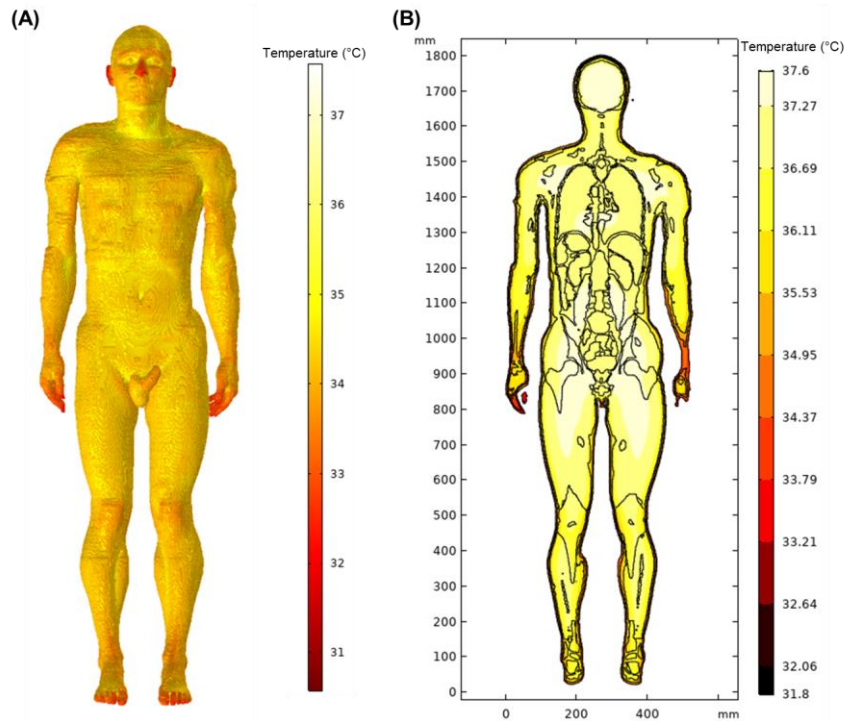


**Figure 4.** The temperature plot for (A) the surface and (B) a coronal slice at  $x = 100$  mm of the modified standard anatomy after stationary temperature simulation with an external temperature of 27°C.

**Table 4.** Average temperatures of the 31 merged tissue types with an external temperature of 27°C.

Merged Index	Merged Tissue type	Average Temperature (°C)
1	Skin	34.61
2	Fat	36.15
3	Muscle / Tendon / Ligament	36.76
4	Bone / Cartilage	36.78
5	Air	36.82
6	Blood	37.00
7	Mucous membrane	37.14
8	Lungs	37.23
9	Heart	37.58
10	Liver	37.17
11	Kidneys	37.08
12	Stomach	37.23
13	Pancreas	37.22
14	Gallbladder	37.20
15	Bladder	37.22
16	Spleen	37.24
17	Large intestine	37.23
18	Small intestine	37.23
19	Esophagus	37.23
20	Trachea	37.15
21	Bronchi	37.17
22	Eyes	36.22
23	Tongue	36.98
24	Brain	37.27
25	Spinal Cord / Nerve	37.22
26	Adrenal gland	37.20
27	Thyroid gland	37.16
28	Thymus	37.21
29	Testis / Epididymis	36.31
30	Prostate	37.25
31	Penis	36.32

## Model Validation

Validation of the model was performed by comparing the simulation with published data. Webb measured the temperatures of several tissues at thermoneutral conditions with an ambient temperature of 27°C (23). The average temperature of the skin and esophagus fall within error bars of the experimentally measured values (Table 5). Additionally, the percent error calculated for each of the measured tissues was less than 6.5% (Table 5).

**Table 5.** Comparison of the simulated temperatures to the measured temperatures from the literature.

Tissue	Simulated temperature (°C)	Measured temperature (°C) (23)	Percent Error
Skin	34.61	33.5 ± 1.3	3.31
Fat	36.15	34.0 ± 1.0	6.32
Muscle	36.76	35.0 ± 1.0	5.03
Esophagus	37.23	36.9 ± 0.4	0.89

## DISCUSSION

The ability to simulate temperature changes of humans is of significant interest to a broad set of communities, including military, clinical areas (public and private), academia (24). The military has a particular interest and investment in developing models that can be used to predict increases in core body temperatures to avoid heat injuries (25, 26) as well as decreases in skin temperatures to avoid cold injuries (24, 27). While the majority of this work for the military has focused on making data-driven predictions based on simple individual or population characteristics (e.g., height, weight); work towards increasing this resolution has been conducted (15, 28).

Mission planning for the military could foreseeably use these models to begin developing computerized groups of simulated Soldier cohorts for scaled simulations that could include both the individual differences while avoid costly and risk-based studies. These simulated cohorts could contain real data based on things such as non-invasive scans of Soldiers or even template data based on computer-generated groups with set differences within their characteristics. For example, increasing accuracy of tissue thickness could lead to more accurate predictions of thermal conductivity and ultimate thermal changes or even steps towards predicting responses injuries (blast, wound, fractures). As stepping stones these models could eventually be envisioned as having the resolution to handle biochemical changes and associated differences within individuals (29, 30). Other benefits related to operational planning could be seen in increased precision of metabolic cost predictions based on body composition differences (31). For metabolic costs, simple methods have been developed to predict gross metabolic costs from (height and weight) (32-34) and some more recent individualized methods have been developed (35-37). Given the high resolution available in these avatars, future work in this area can also be focused on increasing the use and accuracy of more sophisticated modeling. These avatars will have the benefit of being able to validate different outcomes to existing mathematical methods as well as having a platform on which other methods could be implemented onto.

Another future area of work is developing methods or other models that will allow articulation or simulated animation of these types of avatars. Mathematical principles exist that make this conceptual; while the implementation is very complex. Thankfully there have been and continue to be some approaches used to accomplish methods for this (38-43). A critical element for considering the military operational medicine value for these avatars in mission planning is being able to get them to realistically move. These movements can then be combined with energy costs, physiological responses, injury data, etc. and then translated to meaningful tasks to simulate various outcomes.

The approach described herein was only partially successful in identifying proper tissue types for each voxel. To create the model for the thermal simulation, manual segmentation in the volumetric representation was required. With more than 40 million voxels in a single model, even small mismatches or failure to match, can leave many voxels unaccounted for. The approach, therefore, is only a partial solution for creating individualizable finite element models with internal anatomy. Therefore, the next important step is finding solutions for fully automating the process. One solution that

might make this feasible is a commercial software product by Simpleware (i.e. Synopsis Simpleware) (44).

## **CONCLUSIONS**

This work demonstrates the capability of this modeling approach, in conjunction with this type of anatomical data, can be used to produce a mesh avatar that is compatible with thermal simulations. These high resolution simulations compared relatively well with values within the open literature ( $\leq 6.5\%$  error). While the major current limitation to this approach is the significant time investment required for the manual steps; the outline approach within this report show the proof-of-concept for accomplishing the task.

## REFERENCES

1. U.S. Food and Drug Administration Center for Devices and Radiological Health. Reporting of computational modeling studies in medical device submissions: Draft guidance for industry and food and drug administration staff. Sept. 2016.
2. Morrison TM, Pathmanathan P, Adwan M, Margerrison E. Advancing Regulatory Science with Computational Modeling for Medical Devices at the FDA's Office of Science and Engineering Laboratories. *Front Med.* 2018;5:241.
3. Yang KH, Hu J, White NA, King AI, Chou CC, Prasad P. Development of numerical models for injury biomechanics research: a review of 50 years of publications in the Stapp Car Crash Conference. *Stapp Car Crash J.* 2006;50:429-90.
4. Gayzik FS, Moreno DP, Geer CP, Wuertzer SD, Martin RS, Stitzel JD. Development of a Full Body CAD Dataset for Computational Modeling: A Multi-modality Approach. *Ann Biomed Eng.* 2011;39(10):2568-83.
5. Iwamoto M, Nakahira Y, Kimpura H. Development and Validation of the Total HUman Model for Safety (THUMS) Toward Further Understanding of Occupant Injury Mechanisms in Precrash and During Crash. *Traffic Injury Prevention.* 2015;16(sup1):S36-48.
6. Xu T, Sheng X, Zhang T, Liu H, Liang X, Ding A. Development and Validation of Dummies and Human Models Used in Crash Test. *Appl Bionics Biomech.* 2018;2018:3832850.
7. Xu G, Eckerman KF. *Handbook of Anatomical Models for Radiation Dosimetry.* Boca Raton, FL: CRC Press; 2009.
8. DeWerd LA, Kissick M. *The Phantoms of Medical and Health Physics.* New York, NY: Springer; 2014.
9. Xu G. An exponential growth of computational phantom research in radiation protection, imaging and radiotherapy: A review of the fifty-year history. *Phys Med Biol.* 2014;59(18):R233-302.
10. Iacono MI, Neufeld E, Akinagbe E, Bower K, Wolf J, Oikonomidis IV, et al. MIDA: A Multimodal Imaging-Based Detailed Anatomical Model of the Human Head and Neck. *PLoS One.* 2015;10(4):e0124126.
11. Christ A, Kainz W, Hahn EG, Honegger K, Zefferer M, Neufeld E, et al. The virtual family – development of surface-based anatomical models of two adults and two children for dosimetric simulations. *Phys Med Biol.* 2010;55(2):N23-N38.
12. Gosselin M-C, Neufeld E, Moser H, Huber E, Farcito S, Gerber L, et al. Development of a new generation of high-resolution anatomical models for medical device evaluation: the virtual population 3.0. *Phys Med Biol.* 2014;59(18):5287-303.
13. The Virtual Population. Development of a new generation of high-resolution anatomical models for medical device evaluation. In: SPEAG AG, editor. *EuCAP 2016.* Davos, Switzerland, 2016. p. 2.
14. Makarov SN, Noetscher GM, Yanamadala J, Piazza MW, Louie S, Prokop A, et al. Virtual Human Models for Electromagnetic Studies and Their Applications. *IEEE Rev Biomed Eng.* 2017;10:95-121.
15. Zientara GP, Hoyt RW. Individualised avatars with complete anatomy constructed from the ANSUR II 3-D anthropometric database. *Int J Digital Human.* 2016;1(4):389-411.

16. Gordon CC, Blackwell CL, Bradtmiller B, Parham JL, Barrientos P, Paquette SP, et al. 2012 Anthropometric Survey of U.S. Army Personnel: Methods and Summary Statistics. U. S. Army Natick Soldier Research Development and Engineering Center, Natick, MA; 2014. Report No.: TR15/007.
17. Fang Q, Boas D, editors. Tetrahedral mesh generation from volumetric binary and gray-scale images. Proceedings of IEEE International Symposium on Biomedical Imaging 2009; 2009.
18. Fedorov A, Beichel R, Kalpathy-Cramer J, Finet J, Fillion-Robin J-C, Pujol S, et al. 3D Slicer as an image computing platform for the Quantitative Imaging Network. *Magn Reson Imaging*. 2012;30(9):1323-41.
19. Kikinis R, Pieper SD, Vosburgh KG. 3D Slicer: A Platform for Subject-Specific Image Analysis, Visualization, and Clinical Support. In: Jolesz FA, editor. *Intraoperative Imaging and Image-Guided Therapy*. New York, NY: Springer New York; 2014. p. 277-89.
20. Berglund LG, Gonzalez RR, Heled Y, Moran DS. Simulated Human Responses to Transient Cold Wet Sea Exposure Sequences. U. S. Army Research Institute of Environmental Medicine, Natick, MA; 2002 9/2002. Report No.: T02-22.
21. COMSOL Multiphysics®. v 5.4 ed. Stockholm, Sweden: COMSOL AB.
22. IT'IS Database for thermal and electromagnetic parameters of biological tissues, Version 4.0 [Internet]. 2018. Available from: [itis.swiss/database](http://itis.swiss/database).
23. Webb P. Temperatures of skin, subcutaneous tissue, muscle and core in resting men in cold, comfortable and hot conditions. *Eur J Appl Physiol*. 1992;64(5):471-6.
24. Potter A, Looney D, Xu X, Santee W, Srinivasan S. Modeling Thermoregulatory Responses to Cold Environments. *Hypothermia*: IntechOpen; 2018.
25. Potter AW, Blanchard LA, Friedl KE, Cadarette BS, Hoyt RW. Mathematical prediction of core body temperature from environment, activity, and clothing: The heat strain decision aid (HSDA). *J Therm Biol*. 2017;64:78-85.
26. Gonzalez R, McLellan T, Withey W, Chang SK, Pandolf K. Heat strain models applicable for protective clothing systems: comparison of core temperature response. *J Appl Physiol*. 1997;83(3):1017-32.
27. Xu X, Rioux T, Gonzalez J, Hansen E, Castellani J, Santee W, et al. Development of a cold injury prevention tool: The Cold Weather Ensemble Decision Aid (CoWEDA). US Army Research Institute of Environmental Medicine, Natick, MA; 2019. Report No.: T19-06.
28. Xu X, Rioux TP, MacLeod T, Patel T, Rome MN, Potter AW. Measured body composition and geometrical data of four “virtual family” members for thermoregulatory modeling. *Int J Biometeorol*. 2017;61(3):477-86.
29. Slough DP, McHugh SM, Lin YS. Understanding and designing head-to-tail cyclic peptides. *Biopolymers*. 2018;109(10):e23113.
30. Slough DP, McHugh SM, Cummings AE, Dai P, Pentelute BL, Kritzer JA, et al. Designing well-structured cyclic pentapeptides based on sequence–structure relationships. *J Phys Chem B*. 2018;122(14):3908-19.
31. B. Heymsfield S, Wang Z, Baumgartner RN, Ross R. Human body composition: advances in models and methods. *Annu Rev Nutr*. 1997;17(1):527-58.
32. Pandolf KB, Givoni B, Goldman RF. Predicting energy expenditure with loads while standing or walking very slowly. *J Appl Physiol*. 1977;43(4):577-81.

33. Potter AW, Santee WR, Clements CM, Brooks KA, Hoyt RW. Comparative analysis of metabolic cost equations: A review. *J Sport Hum Perf.* 2013;1(3):34-42.
34. Potter AW, Looney DP, Blanchard LA, Welles AP, Santee WR. Accuracy of predictive equations for metabolic cost of locomotion while carrying external load. *J Sport Exerc.* 2017;5(1):1-7.
35. Looney DP, Buller MJ, Gribok AV, Leger JL, Potter AW, Rumpler WV, et al. Estimating resting core temperature using heart rate. *JMPB.* 2018;1(2):79-86.
36. Looney DP, Potter AW, Pryor JL, Bremner PE, Chalmers CR, McClung HL, et al. Metabolic Costs of Standing and Walking in Healthy Military-Age Adults: A Meta-regression. *Med Sci Sports Exerc.* 2019;51(2):346-51.
37. Looney DP, Santee WR, Hansen EO, Bonventre PJ, Chalmers CR, Potter AW. Estimating Energy Expenditure during Level, Uphill, and Downhill Walking. *Med Sci Sports Exerc.* 2019;51(9):1954-60.
38. Boulic R, Bécheiraz P, Emering L, Thalmann D, editors. Integration of motion control techniques for virtual human and avatar real-time animation. *Proceedings of the ACM symposium on Virtual reality software and technology*; 1997.
39. Saragih JM, Lucey S, Cohn JF, editors. Real-time avatar animation from a single image. *Face and Gesture 2011*; 2011: IEEE.
40. Fu Y, Li R, Huang TS, Danielsen M. Real-time multimodal human–avatar interaction. *IEEE Trans Circuits Syst Video Technol.* 2008;18(4):467-77.
41. Thomasset V, Caron S, Weistroffer V, editors. Lower body control of a semi-autonomous avatar in Virtual Reality: Balance and Locomotion of a 3D Bipedal Model. *25th ACM Symposium on Virtual Reality Software and Technology*; 2019.
42. Knopp B, Velychko D, Dreibrodt J, Endres D. Predicting Perceived Naturalness of Human Animations Based on Generative Movement Primitive Models. *ACM T Appl Percept.* 2019;16(3):1-18.
43. Wedig G, Comer SM, Bancroft JJ. Skeletal systems for animating virtual avatars. *Google Patents*; 2019.
44. Castellani MPG, Rioux TP, Potter AW, Xu X. Modeling Male Temperature Profiles with the Finite Element Method and Anatomically Correct Human Torsos. U. S. Army Research Institute of Environmental Medicine, Natick, MA; 2019. Report No.: T19-11.